

Wavefunction textures in twisted bilayer graphene from first principles

Albert Zhu,¹ Daniel Bennett,^{2,*} Daniel T. Larson,³ Mohammed M. Al Ezzi,² Efstratios Manousakis,⁴ and Efthimios Kaxiras^{2,3}

¹Quantum Science and Engineering, Harvard University, Cambridge, Massachusetts 02138, USA

²John A. Paulson School of Engineering and Applied Sciences, Harvard University, Cambridge, Massachusetts 02138, USA

³Department of Physics, Harvard University, Cambridge, Massachusetts 02138, USA

⁴Department of Physics, Florida State University, Tallahassee, Florida 32306, USA

Motivated by recent experiments probing the wavefunctions of magic-angle twisted bilayer graphene (tBLG), we perform large-scale first-principles calculations of tBLG with full atomic relaxation across a wide range of twist angles down to 0.99° . Focusing on the magic angle, we compute wavefunctions of the low energy bands, resolving atomic-scale details and moiré-scale patterns that form triangular, honeycomb, and Kagome lattices. By tuning the interlayer interactions, we illustrate the formation of the flat bands from isolated monolayers and the emergence of the band inversion and fragile topology at a sufficiently large interaction strength. We identify strong indicators of a new topological phase transition with increasing interlayer interaction strength, achievable with external pressure or a decrease in the twist angle. When this transition occurs, the upper and lower flat bands exchange their wavefunction character, which may explain why superconductivity appears with electron doping below the magic angle. Our study demonstrates the feasibility of using first-principles wavefunctions to help interpret experimental signatures of topological and correlated phases in tBLG.

Introduction.—Twisted bilayer graphene (tBLG) near the magic angle has emerged as a prominent platform for studying superconductivity [1–6], correlated insulator behavior [7–11], and topological phenomena such as the anomalous Hall effect [12, 13], Chern insulators [14–17], and fractional Chern insulators [18]. With recent experimental advances, it is possible to measure fundamental properties of tBLG with high precision, providing insight into these exotic phases. For example, quantum twisting microscopy [19] and scanning tunneling microscopy (STM) now allow direct measurement of electronic bands [19], phonons [20] and spatial characteristics of wavefunctions [9], revealing novel orders such as Kekulé spirals and vortex textures [21].

A variety of theoretical methods have been developed to study the electronic structure of magic-angle tBLG [22], ranging from early continuum models [23–26] to more realistic theories, which include *ab initio* tight-binding models [27–30], “exact” $\mathbf{k} \cdot \mathbf{p}$ continuum models [31–36], and minimal phenomenological models that use the smallest number of bands to capture the low-energy physics of tBLG [31, 37–46]. While these approaches provide valuable insight, they rarely capture microscopic details, such as descriptions of the wavefunctions throughout 3D space, necessary for describing the fine features of the wavefunctions observed in STM experiments [9]. First-principles density functional theory (DFT) can resolve these details, but its high computational cost has limited previous studies to large twist angles or specific properties such as atomic relaxation and electronic band structures [47–50]. However, the use of an optimized local basis [51] has allowed us to significantly expand the capabilities of DFT as a tool for studying the wavefunctions of tBLG.

Here, we perform comprehensive DFT calculations of tBLG spanning a wide range of twist angles, from 21.79° down to 0.99° , with supercells containing up to 13,468 atoms, and present results focusing on the microscopic and moiré-scale structure of the low-energy wavefunctions near the

magic angle. Our calculations reveal detailed microscopic and moiré-scale textures in the wavefunctions that can be connected with real-space experimental observations. On the moiré scale, we observe that the wavefunction amplitudes concentrate selectively on the AA, AB/BA, and domain wall (DW) regions, giving rise to distinctive triangular, honeycomb, and Kagome lattices, respectively.

We also examine how interlayer interactions influence the electronic properties of tBLG, demonstrating the onset of band inversion and fragile topology [37, 41, 50, 52]. Notably, we identify the existence of a critical minimum interlayer coupling strength required for the emergence of the band inversion. Furthermore, we discover strong indication of a new topological phase transition occurring at a critical pressure (or twist angle) in which the flat bands touch each other at Γ , resulting in an exchange of wavefunction character between the upper and lower flat bands. This finding can guide experimental measurements of topological phases, and overall, our calculations provide the groundwork for future atomic-scale computational studies of correlated states in tBLG.

Results.—DFT calculations were performed using the SIESTA code [53, 54], which employs a local atomic orbital basis set recently optimized for graphene [51, 55]. After relaxing the atomic structures, the electronic band structures were obtained, as well as the wavefunctions of the flat bands and the neighboring dispersive bands at the Γ , K and M high-symmetry points of the moiré Brillouin zone (mBZ). Fig. 1 shows the Γ -point wavefunction of the lower flat band for tBLG with $\theta = 5.09^\circ$. The microscopic wavefunction probability density $|\Psi|^2$ (Fig. 1 (a)) shows an intricate pattern of bright spots in the AB and BA regions that meet and form interference patterns in the DWs. To visualize the moiré-scale behavior of the wavefunctions, we perform a convolution of $|\Psi|^2$ with a 2D Gaussian [54]. The resulting moiré-scale wavefunction probability density $|\tilde{\Psi}|^2$ exhibits smooth features coinciding with different regions of the moiré pattern, such as a honeycomb lattice shown in Fig. 1 (b) arising from high wavefunction density in the AB and BA domains and low wavefunction density at the AA sites. (In the following,

* dbennett@seas.harvard.edu

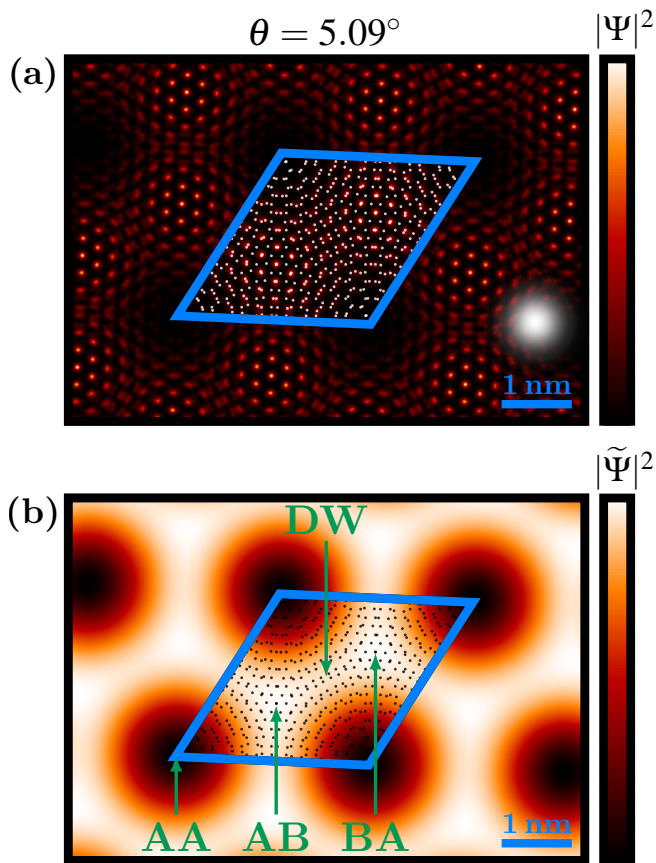


FIG. 1. Wavefunction of tBLG in the lower flat band at Γ for a twist angle of $\theta = 5.09^\circ$. (a) Modulus squared of the atomic-scale wavefunction $|\Psi|^2$, obtained from first-principles calculations. (b) Moiré-scale wavefunction $|\tilde{\Psi}|^2 = |\Psi|^2 * \mathcal{N}$, obtained by a convolution with a Gaussian \mathcal{N} with a standard deviation of 2.5 \AA , sketched above the 1 nm scale bar in (a). The atomic positions are denoted by white and black dots in (a) and (b), respectively. The different stacking regions, AA, AB, BA and domain walls (DW), are labeled in (b).

“wavefunction” will refer to $|\tilde{\Psi}|^2$ unless otherwise specified).

The localization of the wavefunctions depends on both the band and \mathbf{k} -point. To succinctly identify particular wavefunctions, we introduce the following notation: $X_{n\pm}$, where $X = \Gamma, K, M$ represents the high-symmetry \mathbf{k} -points of the mBZ, and $n = 0, 1, 2, \dots$ is the band index, with 0 referring to the flat bands, 1 referring to the first set of dispersive bands, and so on. The sign indicates whether the bands are above (+) or below (−) the charge neutrality point. For example, Γ_{0-} is the lower flat band at Γ , and M_{1+} is the first dispersive conduction band at M . To describe the localization of the wavefunctions, we follow the notation of Ref. [31] and highlight four categories: (i) “AA” wavefunctions that are localized at AA sites and form a triangular lattice, (ii) “ AA_z ” wavefunctions that form rings around AA sites, (iii) “DW” wavefunctions that have weight along domain walls and form a Kagome lattice, and (iv) “AB/BA” wavefunctions that are centered in AB/BA domains and form a honeycomb lattice. All wavefunction plots have color-coded borders correspond-

ing to these four categories, respectively red, blue, green, and pink. Examples of all four are shown in Fig. S1 [54]. Although it is not the focus of this work, we show the evolution of select wavefunctions as a function of twist angle in Fig. S2 [54], with a more detailed analysis to be done in future work.

The wavefunctions of tBLG provide a useful framework to investigate its electronic and topological properties. Although the concepts of fragile topology and band inversion in tBLG are well-established, their physical origin has not been explored; thus, we use the *ab initio* wavefunctions to illustrate how these topological aspects arise as a function of the interlayer interactions. While it is not possible to directly tune the strength of these interactions in DFT calculations, we can instead tune the interlayer spacing. This modifies the vdW interactions between the layers, allowing us to systematically investigate their effect on the electronic properties of tBLG. Fig. 2 shows the evolution of the band structure and Γ -point wavefunctions of magic-angle tBLG ($\theta = 1.08^\circ$) as we systematically interpolate between two flat isolated graphene monolayers and relaxed tBLG. We define the position of an atom in an intermediate structure, \mathbf{r}_n , as a linear interpolation between the corresponding atomic positions in the isolated structure, \mathbf{r}_i , and the fully relaxed structure, \mathbf{r}_f :

$$\mathbf{r}_n = \left(1 - \frac{z_n - z_f}{z_i - z_f}\right) \mathbf{r}_f + \left(\frac{z_n - z_f}{z_i - z_f}\right) \mathbf{r}_i, \quad (1)$$

where z_n is the mean layer separation of the n^{th} interpolated structure, and $z_i = 7.5 \text{ \AA}$ ensures negligible vdW interactions between the flat graphene monolayers. The atomic coordinates \mathbf{r}_n remain fixed during calculations, although we expect the results to qualitatively be unaffected by this construction.

When the graphene layers are isolated, the bands fold into the mBZ, resulting in highly degenerate, delocalized wavefunctions at Γ (Fig. 2, first column). When the layers move closer together and begin to interact, as shown in the second and third columns of Fig. 2, this degeneracy is lifted and two AA wavefunctions emerge, as well as a precursor to the AA_z wavefunction. Decreasing the separation further, the precursor to the AA_z wavefunction shifts up in energy, eventually joining the flat band manifold (fourth column) and localizing in rings around the AA sites in the fully-relaxed structure (last column). Additionally, when the layers are close together, a DW state becomes prominent in the second dispersive band (fourth and last columns).

Band inversion and the opening of mini-gaps between the flat and dispersive bands is a defining feature of the fragile topology of tBLG [37, 41, 50, 52]. We find that a minimum interlayer interaction strength is necessary to lift wavefunction degeneracies and produce the characteristic topological band structure of tBLG. The onset of this band topology, and its dependence on interaction strength, can potentially be probed experimentally using MEGA2D [56]. By adjusting the distance between a graphene sample on a substrate and another graphene sample on the Si pillar, one can potentially tune the interlayer interactions and directly observe these effects.

On the other hand, reducing the twist angle [46] or applying pressure [3, 57, 58] can enhance interlayer interactions and also modify the electronic properties. We simulate the

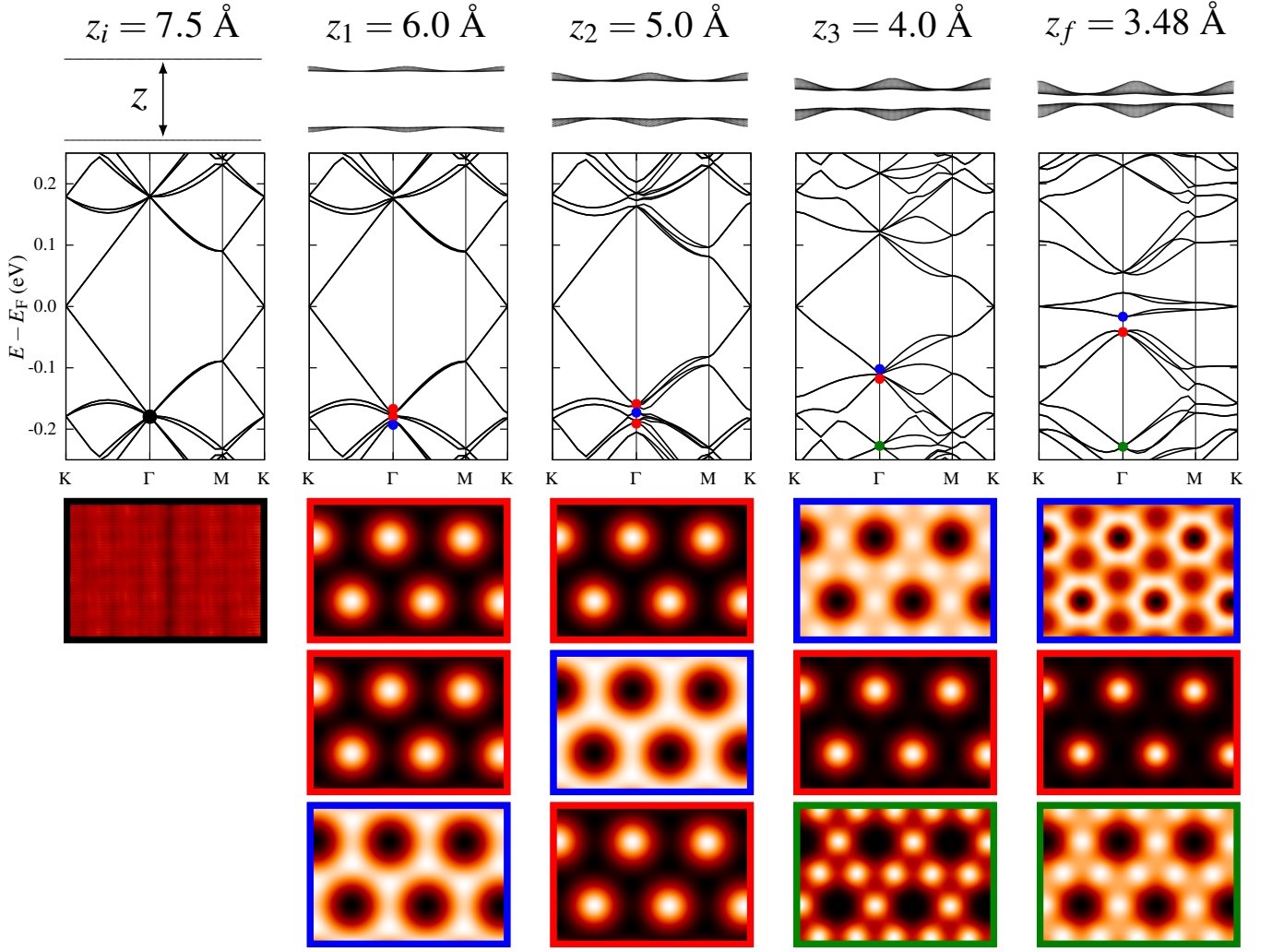


FIG. 2. Emergence of the band inversion in magic-angle tBLG ($\theta = 1.08^\circ$). Each column shows a schematic atomic structure, the band structure, and wavefunctions of the flat bands and dispersive bands for select values of the mean bilayer separation z , which effectively dictates the interlayer interaction strength. The band inversion is demonstrated by the energy of the AA_z state and its precursors at larger z (indicated by blue points in the band structure and blue borders around the wavefunctions) relative to the energy of the AA state(s) (indicated in red) in each column. DW states are indicated in green.

application of pressure by reducing the average layer separation of the relaxed structure of magic-angle tBLG by Δz , allowing us to study the effects of further decreasing the twist angle without performing calculations with even larger supercells [57]. Compressing the layers at the magic angle causes parts of the bands to approach each other, eventually touching and reopening at Γ and M (Fig. 3). The closing and reopening of the energy separation at Γ is accompanied by an exchange of wavefunction character between the upper and lower flat bands throughout the mBZ. The projection of the wavefunction onto layer 1 and sublattice A, $\Psi_{\Gamma_{0\pm}}^{A1}$, shown below the band structure for each value of Δz in Fig. 3, illustrates this exchange at $\Gamma_{0\pm}$. While the total wavefunctions at $\Gamma_{0\pm}$ form ring-like structures around AA sites, the individual projections form structures with threefold symmetry, and the projected wavefunctions of the upper and lower bands

have opposite orientations, denoted by cyan and purple borders. When compression of the layers causes the bands to close and reopen, the orientation of the projected wavefunctions in each band reverses, indicating that their character has been exchanged.

To be more precise, we analyze the eigenvalues of the *microscopic* sublattice-projected wavefunctions under the valley-preserving \mathcal{M}_y symmetry and show that they are exchanged between the upper and lower flat bands after the bands touch and reopen. The \mathcal{M}_y symmetry, which has the effect of exchanging the layers and sublattices, acts on the sublattice-projected wavefunction as follows [32, 37]:

$$\begin{pmatrix} \Psi^{A1}(\mathcal{M}_y \mathbf{r}) \\ \Psi^{B1}(\mathcal{M}_y \mathbf{r}) \\ \Psi^{A2}(\mathcal{M}_y \mathbf{r}) \\ \Psi^{B2}(\mathcal{M}_y \mathbf{r}) \end{pmatrix} \rightarrow \lambda \begin{pmatrix} \Psi^{B2}(\mathbf{r}) \\ \Psi^{A2}(\mathbf{r}) \\ \Psi^{B1}(\mathbf{r}) \\ \Psi^{A1}(\mathbf{r}) \end{pmatrix}, \quad (2)$$

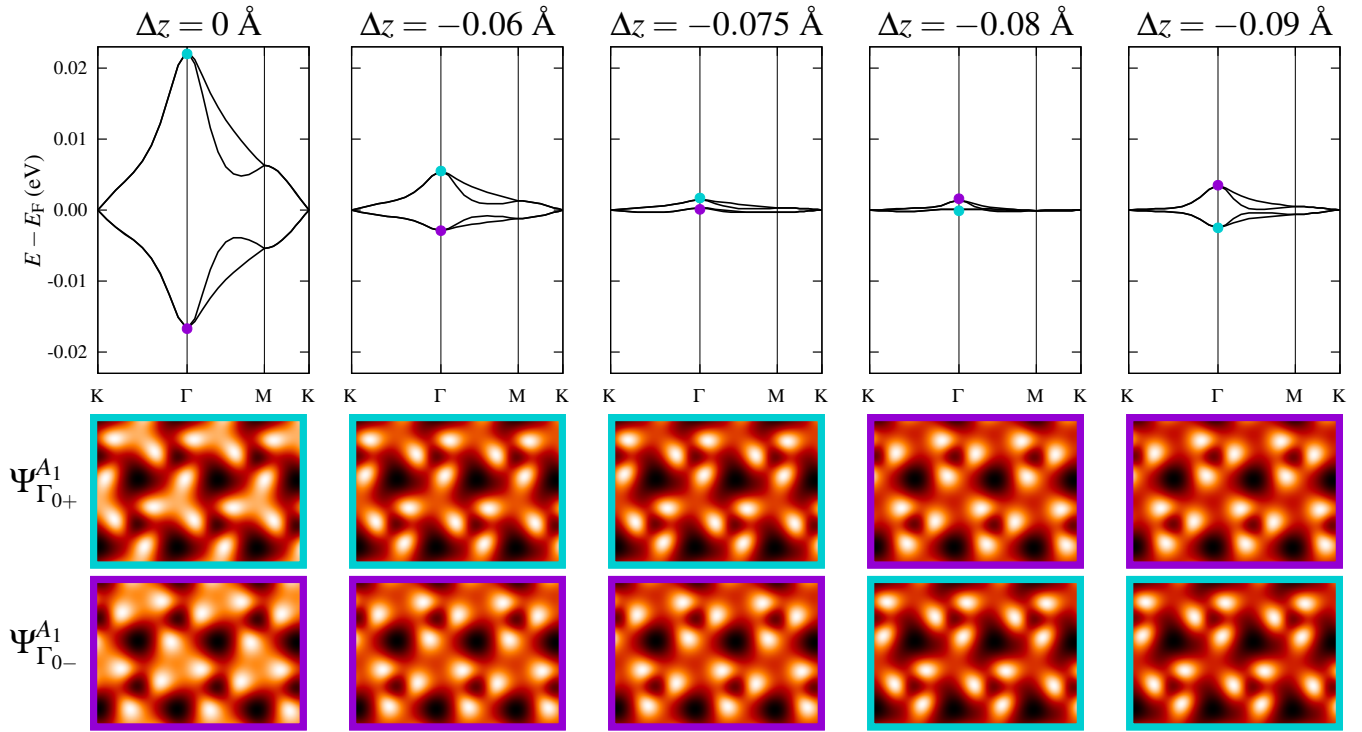


FIG. 3. Electronic band structure and wavefunctions at $\Gamma_{0\pm}$ of magic-angle tBLG as a function of $\Delta z = z - z_f$. The projection of the wavefunction onto layer 1 and sublattice A, $\Psi_{\Gamma_{0\pm}}^{A_1}$, is shown. Cyan and purple borders (and the corresponding points on the band structures) denote wavefunction projections with different orientations.

where $\lambda = \pm 1$ is the mirror eigenvalue. Fig. 4 shows projections of the microscopic wavefunctions at $\Gamma_{0\pm}$ before ($\Delta z = -0.075$ Å) and after ($\Delta z = -0.09$ Å) the closing and reopening of the energy separation. Before the closing, the mirror eigenvalues of the flat bands are $(\lambda_{\Gamma_{0-}}, \lambda_{\Gamma_{0+}}) = (+1, -1)$, and afterwards, they become $(-1, +1)$. In both cases, the mirror eigenvalues in opposite flat bands have opposite sign, meaning the Dirac cones at K and K' have the same chirality, as expected [37], and each eigenvalue changes sign after the transition. We further note that the mirror eigenvalues flip sign not only at Γ but at all \mathbf{k} along Γ -M.

The exchange of orientation and mirror eigenvalues of the wavefunctions between the upper and lower flat bands signals that the closing of the separation at Γ with pressure (or twist angle) is likely a new topological phase transition, as changes in the parity of occupied electronic states are often related to changes in topological invariants [59–61]. While calculation of topological invariants such as the Chern number would explicitly verify the topological nature of this transition, such calculations are still not feasible with DFT and are better suited to simpler models, such as a ten-band tight-binding model [41] fit to the *ab initio* bands, which we defer to future work.

Experimentally, this new topological phase transition should be accessible and tunable with pressure, which effectively scales the twist angle [57], making it possible to induce this transition reversibly in a single device. We estimate this transition to occur in magic angle tBLG at an applied pressure

of 0.5–1 GPa (see Fig. S3 (b) [54]) which can be achieved using a pressure cell [3, 58] or MEGA2D [56]. Since the wavefunction characters of the upper and lower flat bands exchange after the transition, we expect the effects of electron and hole doping to switch with the application of pressure, which should be measurable through transport [3, 58] or microscopy measurements [19]. For example, superconductivity in magic-angle tBLG is observed to be more robust for hole doping than electron doping [62]. However, for a twist angle of 0.93° , below the angle at which the transition is expected to occur [46], superconductivity is only observed with electron doping [8], which may be explained by an exchange of wavefunction character.

Discussion.—We have presented a detailed first-principles characterization of the low-energy wavefunctions of magic-angle tBLG on atomic and moiré scales. Both the microscopic and moiré-scale wavefunctions provide valuable insight into important aspects of the low-energy physics of tBLG, including the dependence of the topology on interlayer interactions. Starting from well separated, noninteracting graphene layers, we have demonstrated two distinct band inversions that occur as the interlayer separation decreases, effectively increasing the interlayer interaction. The first occurs when the flat bands exchange character with the neighboring dispersive bands near Γ : $\Gamma_{0-} \leftrightarrow \Gamma_{1-}$ and $\Gamma_{0+} \leftrightarrow \Gamma_{1+}$. As the interlayer separation is decreased further, the flat bands invert among themselves: $\Gamma_{0-} \leftrightarrow \Gamma_{0+}$. Therefore, this second inversion further entangles bands originating above and below

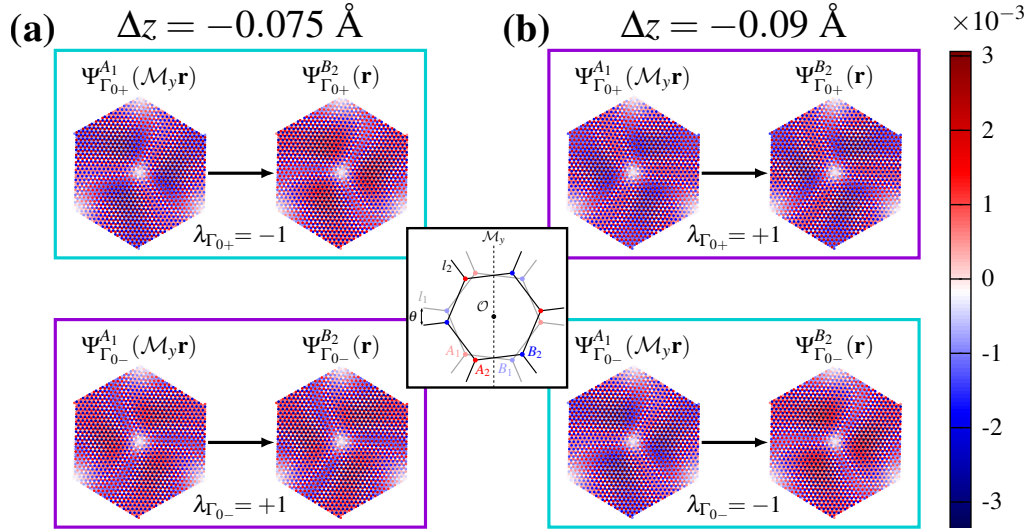


FIG. 4. Transformation of the sublattice-projected microscopic wavefunctions of magic-angle tBLG under the \mathcal{M}_y symmetry (shown in the center). (a) Layer and sublattice projections of the flat band wavefunctions $\Psi_{\Gamma_{0+}}^{A_1}(\mathcal{M}_y \mathbf{r})$ and $\Psi_{\Gamma_{0+}}^{B_2}(\mathbf{r})$ for $\Delta z = -0.075 \text{ \AA}$ with \mathcal{M}_y applied to $\Psi_{\Gamma_{0+}}^{A_1}$. The inverted colors of the wavefunctions show that the upper flat band has a mirror eigenvalue of $\lambda_{\Gamma_{0+}} = -1$. (b) The same as (a), but for $\Delta z = -0.09 \text{ \AA}$. In this case, $\lambda_{\Gamma_{0-}} = -1$.

the Dirac point: $\Gamma_{0-} \leftrightarrow \Gamma_{1+}$ and $\Gamma_{0+} \leftrightarrow \Gamma_{1-}$. Thus, minimal phenomenological models must include complementary bands above *and* below the flat bands to accurately capture the symmetry of the electronic bands of tBLG.

In summary, our first-principles approach provides accurate, atomic-scale, and computationally viable simulations of the microscopic wavefunctions of tBLG with over 10,000 atoms per supercell. This approach will serve as a powerful tool for characterizing the correlated phases observed in STM measurements of the wavefunctions [9], such as intervalley coherent order and Kekulé patterns.

Acknowledgments.—The authors acknowledge support from the Simons Foundation award No. 896626 and the US Army Research Office (ARO) MURI project under Grant

No. W911NF-21-0147. A.Z. is supported by the U.S. Department of Energy, Office of Science, Office of Advanced Scientific Computing Research, Department of Energy Computational Science Graduate Fellowship under Award Number DE-SC0025528. M.M.E.A. acknowledges support from the Singapore Ministry of Education, Research Centre of Excellence Institute for Functional Intelligence Materials. E. M. acknowledges the hospitality of the Harvard Physics Department, where part of this work was done. Computing resources were provided by the Harvard University FAS Division of Science Research Computing Group and the Texas Advanced Computing Center (TACC) at The University of Texas at Austin.

-
- [1] Y. Cao, V. Fatemi, S. Fang, K. Watanabe, T. Taniguchi, E. Kaxiras, and P. Jarillo-Herrero, *Nature* **556**, 43 (2018).
 - [2] X. Lu, P. Stepanov, W. Yang, M. Xie, M. A. Aamir, I. Das, C. Urgell, K. Watanabe, T. Taniguchi, G. Zhang, *et al.*, *Nature* **574**, 653 (2019).
 - [3] M. Yankowitz, S. Chen, H. Polshyn, Y. Zhang, K. Watanabe, T. Taniguchi, D. Graf, A. F. Young, and C. R. Dean, *Science* **363**, 1059 (2019).
 - [4] M. Oh, K. P. Nuckolls, D. Wong, R. L. Lee, X. Liu, K. Watanabe, T. Taniguchi, and A. Yazdani, *Nature* **600**, 240 (2021).
 - [5] M. Tanaka, J. Í.-j. Wang, T. H. Dinh, D. Rodan-Legrain, S. Zaman, M. Hays, A. Almanakly, B. Kannan, D. K. Kim, B. M. Niedzielski, *et al.*, *Nature* **638**, 99 (2025).
 - [6] A. Banerjee, Z. Hao, M. Kreidel, P. Ledwith, I. Phinney, J. M. Park, A. Zimmerman, M. E. Wesson, K. Watanabe, T. Taniguchi, *et al.*, *Nature* **638**, 93 (2025).
 - [7] Y. Cao, V. Fatemi, A. Demir, S. Fang, S. L. Tomarken, J. Y. Luo, J. D. Sanchez-Yamagishi, K. Watanabe, T. Taniguchi, E. Kaxiras, *et al.*, *Nature* **556**, 80 (2018).
 - [8] E. Codecido, Q. Wang, R. Koester, S. Che, H. Tian, R. Lv, S. Tran, K. Watanabe, T. Taniguchi, F. Zhang, *et al.*, *Sci. Adv.* **5**, eaaw9770 (2019).
 - [9] K. P. Nuckolls, R. L. Lee, M. Oh, D. Wong, T. Soejima, J. P. Hong, D. Călugăru, J. Herzog-Arbeitman, B. A. Bernevig, K. Watanabe, *et al.*, *Nature* **620**, 525 (2023).
 - [10] H. Tian, E. Codecido, D. Mao, K. Zhang, S. Che, K. Watanabe, T. Taniguchi, D. Smirnov, E.-A. Kim, M. Bockrath, *et al.*, *Nat. Phys.* **20**, 1407 (2024).
 - [11] R. Krishna Kumar, G. Li, R. Bertini, S. Chaudhary, K. Nowakowski, J. M. Park, S. Castilla, Z. Zhan, P. A. Pantaleón, H. Agarwal, *et al.*, *Nat. Mater.* , 1 (2025).
 - [12] A. L. Sharpe, E. J. Fox, A. W. Barnard, J. Finney, K. Watanabe,

- T. Taniguchi, M. Kastner, and D. Goldhaber-Gordon, *Science* **365**, 605 (2019).
- [13] M. Serlin, C. Tschirhart, H. Polshyn, Y. Zhang, J. Zhu, K. Watanabe, T. Taniguchi, L. Balents, and A. Young, *Science* **367**, 900 (2020).
- [14] K. P. Nuckolls, M. Oh, D. Wong, B. Lian, K. Watanabe, T. Taniguchi, B. A. Bernevig, and A. Yazdani, *Nature* **588**, 610 (2020).
- [15] S. Wu, Z. Zhang, K. Watanabe, T. Taniguchi, and E. Y. Andrei, *Nat. Mater.* **20**, 488 (2021).
- [16] Y. Choi, H. Kim, Y. Peng, A. Thomson, C. Lewandowski, R. Polski, Y. Zhang, H. S. Arora, K. Watanabe, T. Taniguchi, *et al.*, *Nature* **589**, 536 (2021).
- [17] P. Stepanov, M. Xie, T. Taniguchi, K. Watanabe, X. Lu, A. H. MacDonald, B. A. Bernevig, and D. K. Efetov, *Phys. Rev. Lett.* **127**, 197701 (2021).
- [18] Y. Xie, A. T. Pierce, J. M. Park, D. E. Parker, E. Khalaf, P. Ledwith, Y. Cao, S. H. Lee, S. Chen, P. R. Forrester, *et al.*, *Nature* **600**, 439 (2021).
- [19] A. Inbar, J. Birkbeck, J. Xiao, T. Taniguchi, K. Watanabe, B. Yan, Y. Oreg, A. Stern, E. Berg, and S. Ilani, *Nature* **614**, 682 (2023).
- [20] J. Birkbeck, J. Xiao, A. Inbar, T. Taniguchi, K. Watanabe, E. Berg, L. Glazman, F. Guinea, F. von Oppen, and S. Ilani, *Nature*, 1 (2025).
- [21] Y. H. Kwan, G. Wagner, T. Soejima, M. P. Zaletel, S. H. Simon, S. A. Parameswaran, and N. Bultinck, *Phys. Rev. X* **11**, 041063 (2021).
- [22] S. Carr, S. Fang, and E. Kaxiras, *Nat. Rev. Mater.* **5**, 748 (2020).
- [23] J. M. B. Lopes dos Santos, N. M. R. Peres, and A. H. Castro Neto, *Phys. Rev. Lett.* **99**, 256802 (2007).
- [24] R. Bistritzer and A. H. MacDonald, *PNAS* **108**, 12233 (2011).
- [25] E. J. Mele, *Phys. Rev. B* **84**, 235439 (2011).
- [26] J. M. B. Lopes dos Santos, N. M. R. Peres, and A. H. Castro Neto, *Phys. Rev. B* **86**, 155449 (2012).
- [27] G. Trambly de Laissardière, D. Mayou, and L. Magaud, *Nano Lett.* **10**, 804 (2010).
- [28] J. Jung and A. H. MacDonald, *Phys. Rev. B* **89**, 035405 (2014).
- [29] S. Fang and E. Kaxiras, *Phys. Rev. B* **93**, 235153 (2016).
- [30] S. Carr, D. Massatt, S. Fang, P. Cazeaux, M. Luskini, and E. Kaxiras, *Phys. Rev. B* **95**, 075439 (2017).
- [31] S. Carr, S. Fang, Z. Zhu, and E. Kaxiras, *Phys. Rev. Res.* **1**, 013001 (2019).
- [32] S. Fang, S. Carr, Z. Zhu, D. Massatt, and E. Kaxiras, *arXiv:1908.00058* (2019).
- [33] F. Guinea and N. R. Walet, *Phys. Rev. B* **99**, 205134 (2019).
- [34] J. Kang and O. Vafek, *Phys. Rev. B* **107**, 075408 (2023).
- [35] O. Vafek and J. Kang, *Phys. Rev. B* **107**, 075123 (2023).
- [36] W. Miao, C. Li, X. Han, D. Pan, and X. Dai, *Phys. Rev. B* **107**, 125112 (2023).
- [37] L. Zou, H. C. Po, A. Vishwanath, and T. Senthil, *Phys. Rev. B* **98**, 085435 (2018).
- [38] H. C. Po, L. Zou, A. Vishwanath, and T. Senthil, *Phys. Rev. X* **8**, 031089 (2018).
- [39] M. Koshino, N. F. Q. Yuan, T. Koretsune, M. Ochi, K. Kuroki, and L. Fu, *Phys. Rev. X* **8**, 031087 (2018).
- [40] J. Kang and O. Vafek, *Phys. Rev. X* **8**, 031088 (2018).
- [41] H. C. Po, L. Zou, T. Senthil, and A. Vishwanath, *Phys. Rev. B* **99**, 195455 (2019).
- [42] G. Tarnopolsky, A. J. Kruchkov, and A. Vishwanath, *Phys. Rev. Lett.* **122**, 106405 (2019).
- [43] S. Carr, S. Fang, H. C. Po, A. Vishwanath, and E. Kaxiras, *Phys. Rev. Res.* **1**, 033072 (2019).
- [44] B. A. Bernevig, Z.-D. Song, N. Regnault, and B. Lian, *Phys. Rev. B* **103**, 205411 (2021).
- [45] Z.-D. Song and B. A. Bernevig, *Phys. Rev. Lett.* **129**, 047601 (2022).
- [46] D. Bennett, D. T. Larson, L. Sharma, S. Carr, and E. Kaxiras, *Phys. Rev. B* **109**, 155422 (2024).
- [47] K. Uchida, S. Furuya, J.-I. Iwata, and A. Oshiyama, *Phys. Rev. B* **90**, 155451 (2014).
- [48] P. Lucignano, D. Alfè, V. Cataudella, D. Ninno, and G. Cantele, *Phys. Rev. B* **99**, 195419 (2019).
- [49] K. Yananose, G. Cantele, P. Lucignano, S.-W. Cheong, J. Yu, and A. Stroppa, *Phys. Rev. B* **104**, 075407 (2021).
- [50] Z. Song, Z. Wang, W. Shi, G. Li, C. Fang, and B. A. Bernevig, *Phys. Rev. Lett.* **123**, 036401 (2019).
- [51] D. Bennett, M. Pizzochero, J. Junquera, and E. Kaxiras, *Phys. Rev. B* **111**, 125123 (2025).
- [52] J. Ahn, S. Park, and B.-J. Yang, *Phys. Rev. X* **9**, 021013 (2019).
- [53] J. M. Soler, E. Artacho, J. D. Gale, A. García, J. Junquera, P. Ordejón, and D. Sánchez-Portal, *J. Phys. Condens. Matter* **14**, 2745 (2002).
- [54] See Supplementary Material for more details.
- [55] J. Junquera, O. Paz, D. Sánchez-Portal, and E. Artacho, *Phys. Rev. B* **64**, 235111 (2001).
- [56] H. Tang, Y. Wang, X. Ni, K. Watanabe, T. Taniguchi, P. Jarillo-Herrero, S. Fan, E. Mazur, A. Yacoby, and Y. Cao, *Nature* **632**, 1038 (2024).
- [57] S. Carr, S. Fang, P. Jarillo-Herrero, and E. Kaxiras, *Phys. Rev. B* **98**, 085144 (2018).
- [58] M. Yankowitz, J. Jung, E. Laksono, N. Leconte, B. L. Chittari, K. Watanabe, T. Taniguchi, S. Adam, D. Graf, and C. R. Dean, *Nature* **557**, 404 (2018).
- [59] L. Fu and C. L. Kane, *Phys. Rev. B* **76**, 045302 (2007).
- [60] C. Fang, M. J. Gilbert, and B. A. Bernevig, *Phys. Rev. B* **86**, 115112 (2012).
- [61] J. Kruthoff, J. de Boer, J. van Wezel, C. L. Kane, and R.-J. Slager, *Phys. Rev. X* **7**, 041069 (2017).
- [62] L. Balents, C. R. Dean, D. K. Efetov, and A. F. Young, *Nat. Phys.* **16**, 725 (2020).
- [63] D. Hamann, *Phys. Rev. B* **88**, 085117 (2013).
- [64] A. García, M. J. Verstraete, Y. Pouillon, and J. Junquera, *Comput. Phys. Commun.* **227**, 51 (2018).
- [65] M. Van Setten, M. Giantomassi, E. Bousquet, M. J. Verstraete, D. R. Hamann, X. Gonze, and G.-M. Rignanese, *Comput. Phys. Commun.* **226**, 39 (2018).
- [66] J. P. Perdew, K. Burke, and M. Ernzerhof, *Phys. Rev. Lett.* **77**, 3865 (1996).
- [67] S. Grimme, J. Antony, S. Ehrlich, and H. Krieg, *J. Chem. Phys.* **132** (2010).

Supplemental Material

S1. FIRST-PRINCIPLES CALCULATIONS

First-principles density functional theory (DFT) calculations were performed using the SIESTA [53] code, version 5.0, with norm-conserving [63] PSML pseudopotentials [64], obtained from Pseudo-Dojo [65]. SIESTA uses a basis of numerical atomic orbitals (NAOs) [55], and a basis optimized for graphene from Ref. [51] was used in all calculations. In order to keep the calculations efficient, a basis of single- ζ polarized (SZP) orbitals were used for all calculations, with $2s$, $2p$ orbitals for each carbon atom, and $3d$ polarization orbitals. The optimized basis set made it possible to perform efficient and accurate full first-principles calculations for tBLG for twist angles as low as $\theta = 0.99^\circ$ (13,468 atoms).

The PBE exchange-correlation functional [66] was used in all calculations, and a DFT-D3 dispersion correction [67] was included in order to treat the long range interactions between the layers. A single \mathbf{k} -point was used in all calculations, and the real space grid was determined using an energy cutoff of 300 Ry. Calculations were performed using the MRRR solver for geometry relaxations, including only the first 20 conduction bands above the Fermi level. The SCF was converged until the relative changes in the density matrix were below 10^{-4} .

Commensurate twisted bilayer structures were generated for twist angles from $\theta = 21.79^\circ$ down to $\theta = 0.99^\circ$. Starting with two flat layers with a layer separation of $d = 3.35 \text{ \AA}$, the atomic positions were relaxed until the forces on all atoms were below the force tolerance. A force tolerance of 1 meV/\AA was used for larger twist angles (smaller supercells), but was increased up to 10 meV/\AA for the smaller twist angles (larger supercells) in the interest of computational efficiency. The center of mass was fixed in the out-of-plane direction in order to prevent the bilayer from drifting from its initial position in middle of the cell. After the relaxed geometries were obtained, calculations were performed to obtain the electronic band structures. The default solver was used for these calculations, and all bands were included. The bands were obtained along the path $\text{K}-\Gamma-\text{M}-\text{K}$, with 10 points along each segment.

S2. WAVEFUNCTIONS

We obtain three-dimensional real-space wavefunctions $\Psi_{n\mathbf{k}}(\mathbf{r})$ for the low-energy bands n at the high-symmetry \mathbf{k} points Γ , M, and K, in the mBZ. In SIESTA, atomic-scale wavefunctions are represented as linear combinations of the local (non-orthogonal) basis orbitals ϕ_μ :

$$\Psi_{n\mathbf{k}}(\mathbf{r}) = \sum_{\mu} c_{n\mathbf{k},\mu} \phi_{\mu}(\mathbf{r}). \quad (\text{S1})$$

Additionally, we obtain sublattice-projected wavefunctions by calculating the projection of $\Psi_{n\mathbf{k}}$ onto the basis orbitals of a specific layer and sublattice $s \in \{A_1, A_2, B_1, B_2\}$:

$$\Psi_{n\mathbf{k}}^s(\mathbf{r}) = \sum_{\mu \in s} c_{n\mathbf{k},\mu} \phi_{\mu}(\mathbf{r}). \quad (\text{S2})$$

In order to obtain a two-dimensional representation of $\Psi_{n\mathbf{k}}(\mathbf{r})$, we show the modulus squared of the wavefunction, averaged in the out-of-plane direction z : $|\Psi_{n\mathbf{k}}(x, y)|^2 = \sum_z |\Psi_{n\mathbf{k}}(x, y, z)|^2$. For degenerate states, we add the moduli squared of the degenerate wavefunctions. To visualize the moiré-scale features of the atomic-scale wavefunctions, we perform a convolution

$$(f * g)(\mathbf{r}) = \int f(\mathbf{r}') g(\mathbf{r} - \mathbf{r}') d\mathbf{r}' \quad (\text{S3})$$

of $|\Psi_{n\mathbf{k}}(x, y)|^2$ with a symmetric two-dimensional Gaussian filter. The moiré-scale wavefunction $|\tilde{\Psi}_{n\mathbf{k}}|^2$ is given by

$$|\tilde{\Psi}_{n\mathbf{k}}|^2(x, y) \equiv (|\Psi_{n\mathbf{k}}|^2 * \mathcal{N})(x, y) = \sum_{x', y'} |\Psi_{n\mathbf{k}}(x', y')|^2 \mathcal{N}_{x, y}(x', y'). \quad (\text{S4})$$

Here, $\mathcal{N}_{x, y}(x', y')$ denotes the probability density function of a Gaussian with mean (x, y) and covariance matrix $\sigma^2 I_{2 \times 2}$ evaluated at the point (x', y') . In practice, we sum over all (x', y') such that $\|(x', y') - (x, y)\| \leq 3\sigma$. We set σ on the order of 1 to 10 \AA , just large enough to clearly extract the moiré-scale features of the wavefunctions, and generally choose larger σ for larger supercells (smaller θ). For example, $\sigma = 2.5 \text{ \AA}$ for $\theta = 5.09^\circ$ in Fig. 1 in the main text, while $\sigma = 10 \text{ \AA}$ for $\theta = 1.08^\circ$ in Fig. 2 and 3 in the main text.

Fig. S1 shows the different wavefunction characters mentioned in the main text (AA, AA_z, AB/BA, and DW) for $\theta = 0.99^\circ$. Fig. S2 shows the evolution of the microscopic and moiré-scale wavefunctions at Γ_{0-} as a function of twist angle.

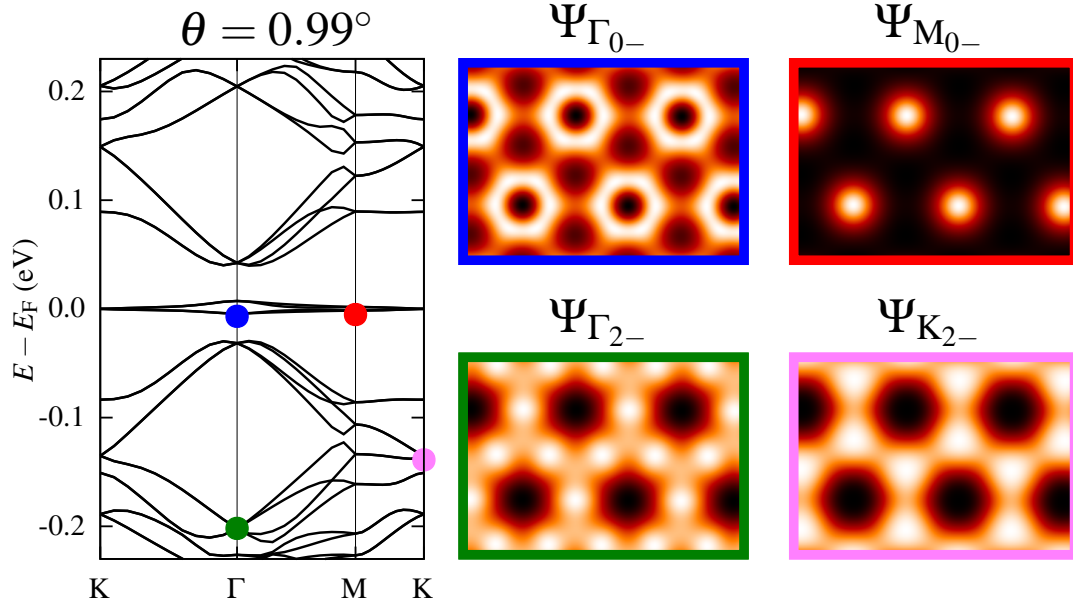


FIG. S1. Representative wavefunctions for a twist angle of $\theta = 0.99^\circ$. AA, AA_z, AB/BA, and DW wavefunctions are outlined in red, blue, pink, and green, respectively.

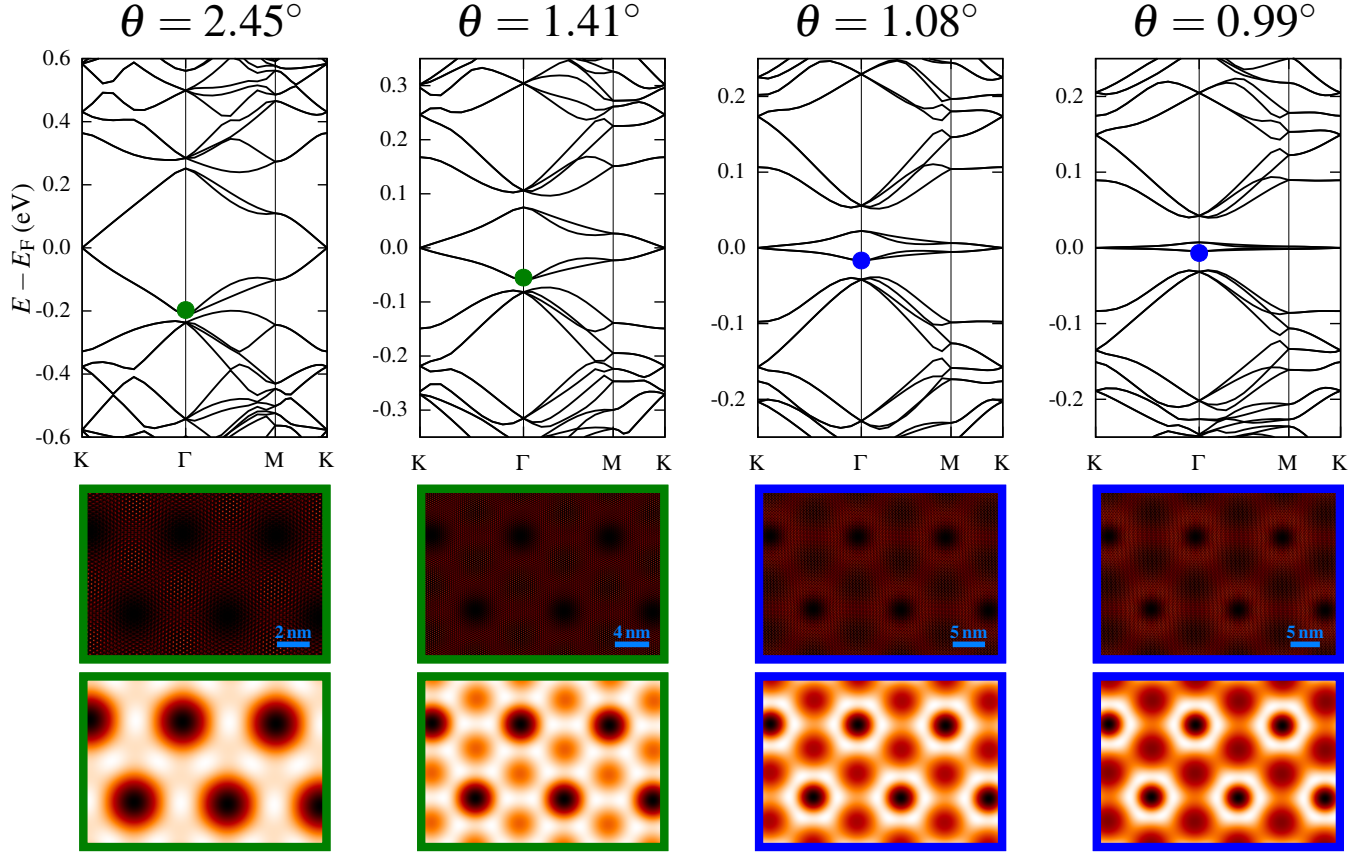


FIG. S2. Electronic band structures and wavefunctions at Γ_{0-} as a function of twist angle θ , with the top row of wavefunction panels showing the microscopic textures and the bottom row showing the moiré-scale features. The color of the circles on the band structures and the borders of the wavefunctions indicates the character of the wavefunctions as described in the main text.

S3. ESTIMATION OF PRESSURE

The energy of magic-angle tBLG is shown as a function of average layer separation in Fig. S3 (a), for a small variation Δz about the equilibrium value $z_f = 3.48 \text{ \AA}$. For each value of Δz , the atomic coordinates were held fixed and a single point calculation was performed. We note that the minimum in energy is not exactly at z_f . Due to the large number of degrees of freedom, a very low force tolerance is required to find the true minimum, and the initial relaxation was performed with a force tolerance of 10 meV/\AA in the interest of computational efficiency.

An equation of state was used to fit the data and calculate the bulk modulus:

$$B = V_f \frac{d^2 E}{dV^2} = \frac{z_f}{A} \left. \frac{d^2 E}{dz^2} \right|_{z=z_f}, \quad (\text{S5})$$

where E is the energy, $V = Az$ is the volume, and A is the in-plane area and $z = z_f + \Delta z$. A quadratic fit,

$$E(z) = \frac{1}{2} V_f B (z - z_0)^2, \quad (\text{S6})$$

where z_0 is the energy minimum, is shown in Fig. S3 in red, which yields a bulk modulus of $B = 24.95 \text{ GPa}$. A Birch-Murnaghan equation of state,

$$E(z) = \frac{9}{16} V_f B \left\{ \left[\left(\frac{z_f}{z} \right)^{2/3} - 1 \right]^3 B' + \left[\left(\frac{z_f}{z} \right)^{2/3} - 1 \right]^2 \left[6 - 4 \left(\frac{z_f}{z} \right)^{2/3} \right] \right\}, \quad (\text{S7})$$

where B' is the derivative of the bulk modulus, is shown in Fig. S3 in blue, yielding a bulk modulus of $B = 21.41 \text{ GPa}$. The Birch-Murnaghan equation of state yields a better fit to the data, as it captures the asymmetry about $\Delta z = 0$.

The induced pressure ΔP as a function of Δz ,

$$\Delta P = -\frac{E}{V_f} \approx -B \frac{\Delta z}{z_f}, \quad (\text{S8})$$

is shown in Fig. S3 (b). The solid lines show the linear approximation obtained using the bulk modulus, and the dashed lines show the induced pressure obtained from the derivative of the energy. For the quadratic fit, the two methods match exactly. For the Birch-Murnaghan fit, some nonlinearity is induced. The vertical line shows the approximate $\Delta z/z_f$ required to induce the topological phase transition described in the main text. We can see that all estimations indicate a pressure in the range $0.5 \text{ GPa} < \Delta P < 1.0 \text{ GPa}$ is required to induce this transition.

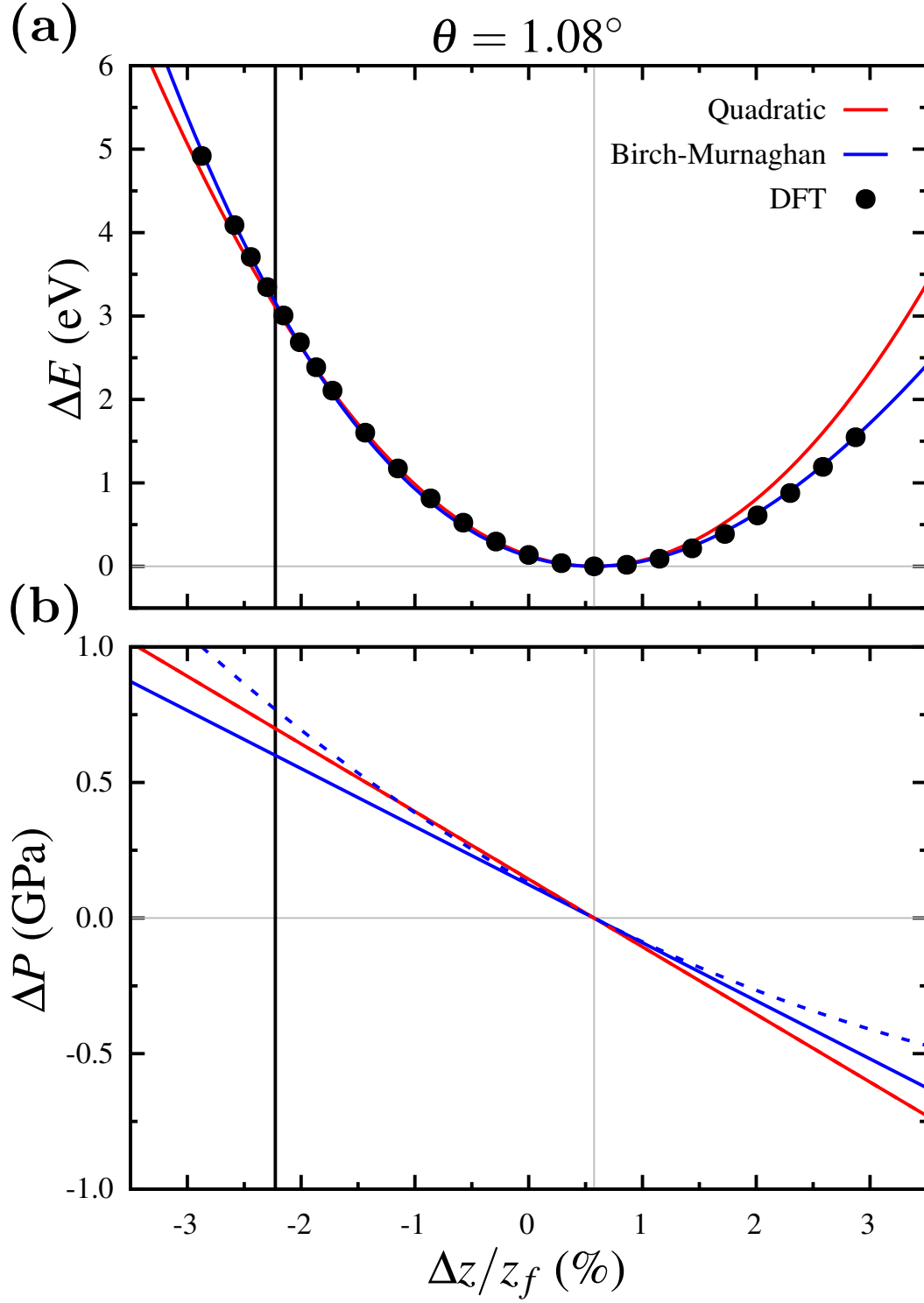


FIG. S3. **(a)** Energy as a function of average layer separation for magic-angle tBLG. The black circles indicate results from DFT calculations. The red and blue lines show fits using quadratic and Birch-Murnaghan equations of state, respectively. **(b)** Pressure as a function of layer separation for magic-angle tBLG. The solid lines show the linear approximation using the bulk modulus calculated from the fitting in (a). The dashed lines show the pressure obtained by differentiating the energy. The vertical black line in each plot denotes the value of $\Delta z/z_f$ at which the flat bands touch each other at Γ .